Available online at www.sciencedirect.com
SCIENCE DIRECT®
Journal of Power Sources 139 (2005) 115–125
JOURNAL OF POWER SOURCES
www.elsevier.com/locate/jpowsour

Predictions of internal temperature distribution of PEMFC by non-destructive inverse method

Chin-Hsiang Cheng*, Mei-Hsia Chang

Department of Mechanical Engineering, Tatung University, 40 Chungshan N. Road, Section 3, Taipei, Taiwan 10451, ROC

Received 14 June 2004; accepted 30 June 2004
Available online 11 September 2004

Abstract

A non-destructive inverse method is applied to predict the global temperature distribution at the interface between the carbon plate and the membrane electrode assembly of a proton exchange membrane fuel cell (PEMFC) based on the measured temperature data on the outer surface of the end plate. A direct problem solver is built to provide temperature solutions for various physical conditions and is then incorporated with the conjugate gradient method to develop an inverse method for temperature prediction. Three specified functions are taken as exact temperature distributions at the interfaces and are predicted by using the inverse method. The validity of the inverse approach is demonstrated by investigating the effects of the number and locations of the measurement points and the experimental uncertainty on the accuracy of the predicted solutions. In addition, the possibility of internal temperature prediction based on the temperature data on the edges of the carbon plate is also studied. Results show that the inner surface temperatures of the carbon plates in contact with the MEA is possible to be determined based on the measured temperature data on the outer surfaces.

Keywords: Inverse method; Non-destructive measurement; Fuel cell; Temperature distribution

1. Introduction

Proton exchange membrane fuel cells (PEMFCs) have been developed to provide electricity for a variety of stationary and transportation applications. In order to produce commercially viable units, it would be necessary to pursue further research in the areas of water and thermal management [1–4], cell stacking processes [5–7], designs for bipolar plates and flow-fields [8,9], and fuel processing [10,11].

PEMFC modeling can help advance this technological development by facilitating the understanding of the physico-chemical and heat transfer phenomena occurring in a fuel cell. Furthermore, these modeling studies provide a valuable tool for the optimization of the structure as well as the geometry and the operation conditions of the fuel cell stacks. For example, Yuan et al. [12] simulated a fully developed laminar flow and heat transfer process in the carbon plate channel with rectangular or trapezoidal cross section and a permeable porous wall. Kumar and Reddy [13], on the other hand, focused on the improvement of the performance of the PEMFC by optimizing the channel dimensions and shape in the flow-field of bipolar/end plates. Lately, Um and Wang [14] used a computational fuel cell dynamics (CFCD) model to study electrochemical kinetics, current density distribution, fuel and oxidant flow, and multi-component transport in a PEM fuel cell with cathode carbon plate having straight or interdigitated air channels.

Since the electrical energy produced by a fuel cell is accompanied by a nearly equal amount of thermal energy, the generated heat is required to keep the working temperatures of the fuel cells within safe levels. Without proper thermal management, the performance of the fuel cells may not be maintained. A too high cell temperature, even in confined areas, may lead to membrane dehydration, and a too low cell

* Corresponding author. Tel.: +886 2 25925252x3410; fax: +886 2 25997142.
E-mail address: cheng@ttu.edu.tw (C.-H. Cheng).

0378-7753/$ – see front matter © 2004 Elsevier B.V. All rights reserved.
doi:10.1016/j.jpowsour.2004.06.070

Nomenclature

a_i (i = 0, . . ., 5) undetermined coefficients of temperature function
C heat capacity (kJ(kg °C)$^{-1}$)
h heat transfer coefficient (W (m^2 °C)$^{-1}$)
H height (m)
$\overline{j}$ specific objective function
J objective function
k thermal conductivity (W (m °C)$^{-1}$)
L length of fuel cell (m)
$\overline{m}, \overline{n}$ number of temperature measurement points on outer surface in x- and y-direction
NX, NY, NZ numbers of grid points in x-, y-, and z-direction
q^* internal heat source (W m^{-3})
r random number varied between −1 and 1
t time (s)
T temperature of fuel cell (°C)
$\overline{T}$ simulated experimental outer surface temperature data (°C)
T_a ambient temperature (°C)
W width of fuel cell (m)
x, y, z Cartesian coordinates (m)

Greek symbols
β step size
ε error norm (°C)
γ conjugate gradient coefficient
π search direction
θ exact temperature function at MEA/carbon plate interface (°C)
ρ density (kg m^{-3})
σ uncertainty of temperature measurement

Subscripts
C carbon plate
Cu copper plate
e end plate
ex exact solution
g gasket
i, j, k grid point indices
I, J temperature measurement point indices

Superscript
n iteration step

temperature may result in water condensation or even flooding. In order to ensure proper thermal management for the fuel cell, it is essential to predict the temperature distribution inside the fuel cell. However, it is the surface temperature of the fuel cell that can be readily measured, and the temperature inside the fuel cell is usually difficult to determine. Or alternatively, to measure the internal temperature of a fuel cell, one may use destructive methods in which a number of temperature sensors are inserted into the fuel cell directly. Unfortunately, the destructive methods actually damage the structure of the fuel cell to a certain extent and disturb the flow and current fields inside the fuel cell. In these circumstances, a non-destructive method which can be applied in determination of the internal temperature of a fuel cell is required.

In this study, an inverse concept is proposed for obtaining the global temperature distribution inside the fuel cell at the interface between the MEA and the carbon plate. This method features the major advantage of producing no destructive effects on the fuel cell structure. With the present method, the interface temperature distribution between the carbon plate and the MEA is determined based on the temperature measurement of the outer surface of the end plate. The validity of the present inverse method is tested by a number of simulated cases.

Fig. 1 shows the schematic of a single cell of the PEMFC and its physical model as well. The PEMFC for a single cell shown in this figure consists of a polymer electrolyte, which

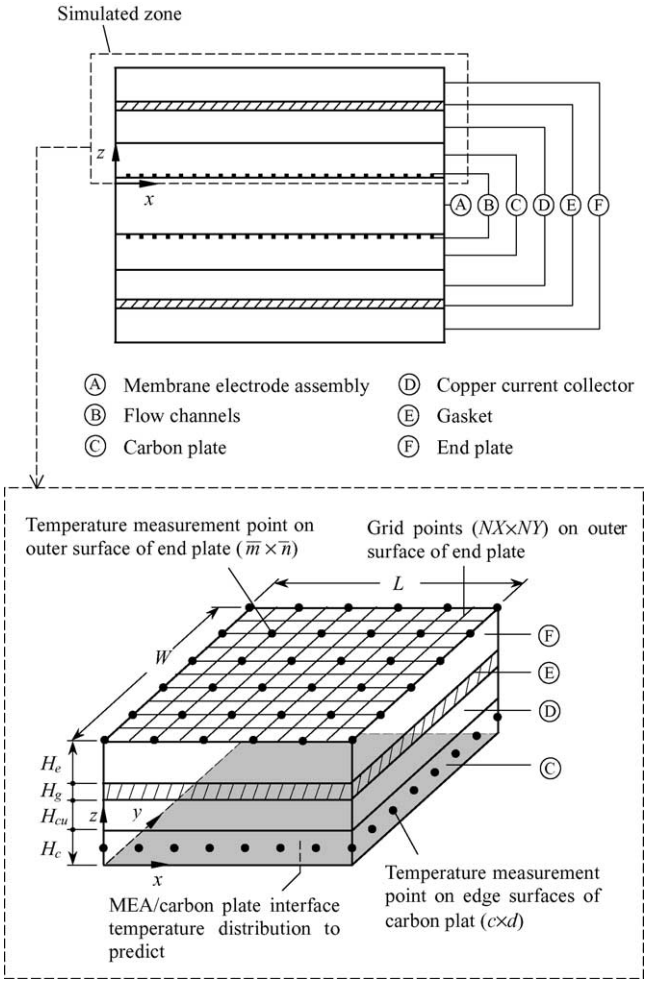

Fig. 1. Physical model for a single-cell PEMFC.

Table 1
Fixed dimensions, material properties, and surface conditions of the test cases

	Carbon plate	Copper plate	Gasket	End plate
L	0.21	0.21	0.21	0.21
W	0.21	0.21	0.21	0.21
H	0.003	0.003	0.0003	0.004
k	95	380	0.17	200
h	10[a]	10[a]	10[a]	10[b]
T_a	25[a]	25[a]	25[a]	25[b]

[a] Edge convection.
[b] Outer surface and edge convection.

is sandwiched between two electrodes and two gas diffusion layers to form a five-layer MEA. The five-layer MEA is placed between two carbon plates with machined grooves that provide flow channels for distributing fuel and oxidant gases. The inner face of each of the carbon plates is in contact with the MEA, and the temperature distribution on the inner surface of the carbon plate is to be determined in the study. The outer faces of the carbon plates are in contact with two respective copper current collectors, which are insulated by two gaskets from the outside. Finally, the structure is clamped tightly between two end plates. The geometric conditions of the materials of the components considered in the study are listed in Table 1. As the fuel cell is in operation, heat is generated from the electrochemical reaction and conducted toward the outer surfaces, and then dissipated to the ambient air at temperature T_a by convection. The heat transfer coefficient on all the outer surfaces of the fuel cell is denoted by h. An array of temperature sensors is installed on the outer surface of the end plate or on the edge surfaces of the carbon plate to measure the surface temperatures. However, note that the temperature distribution on the outer surface of the end plate can also be detected by using an infrared radiation thermal image system. The effects of the number and locations of the temperature measurement points and the experimental uncertainty are among the major issues investigated in this study.

2. Optimization method

2.1. Heat conduction problem solver

The materials of the components, including the carbon plate, the copper plate, the gasket, and the end plate, used in the fuel cell are assumed to be homogeneous and isotropic. Therefore, heat conduction within these solid layers is governed by the following partial differential equation:

$$\rho C \frac{\partial T}{\partial t} = k\nabla^2 T + q^* \tag{1}$$

where q^* denotes the internal heat source; ρ, C, and k are the density, heat capacity, and thermal conductivity of the solid materials, respectively; and T is the temperature. The present approach is mainly concerned with the steady thermal behavior; therefore, the three-dimensional steady-state heat conduction equation for all the solid materials is expressed as follows:

$$\frac{\partial^2 T}{\partial x^2} + \frac{\partial^2 T}{\partial y^2} + \frac{\partial^2 T}{\partial z^2} = 0 \tag{2}$$

Note that the MEA is not necessarily to be included in the present modeling since the solution domain is confined between the outer surface and the MEA/carbon plate interface. The boundary conditions associated with Eq. (2) are:

(a) On outer surfaces:

$$\pm k \frac{\partial T}{\partial n} = h[T - T_a] \tag{3a}$$

where n is the coordinate normal to the individual outer surfaces.

(b) At interface between any two solid layers:

$$T_1 = T_2 \tag{3b}$$

$$k_1 \frac{\partial T_1}{\partial n_1} = k_2 \frac{\partial T_2}{\partial n_2} \tag{3c}$$

where the subscripts 1 and 2 denote any two solid layers in contact.

Eqs. (2) and (3) can be transformed into a set of simultaneous algebraic equations for the temperature solutions at all the grid points by using the finite-difference method. With the help of the successive-over-relaxation method (SOR) [15], the convergent numerical solution for the three-dimensional temperature distribution within the entire fuel cell (with NX × NY × NZ grid points) can be obtained. Note that NZ is the sum of NZ_C, NZ_{Cu}, NZ_g, and NZ_e, the numbers of grid points in Z-direction within carbon plate, copper current collector, gasket, and end plate. Fixed physical variables used in computation are listed in Table 1.

2.2. Conjugate gradient method

The temperature measurement data on the outer surface of the end plate are denoted by $\overline{T}_{I,J}$ ($I = 1 \sim \overline{m}$, and $J = 1 \sim \overline{n}$). Let $T_{i,j,NZ}$ denote the numerical temperature solution at the grid point (i, j, NZ) with $i = 1 \sim NX$, $j = 1 \sim NY$, and $k = NZ$, which is on the outer surface of the end plate. The number of the measured temperature points ($\overline{m} \times \overline{n}$) can be less than or equal to the number of grid points (NX × NY) on the outer

Table 2
Exact solutions at MEA/carbon plate interface for the test cases

Case	Exact solution
1	$\theta(x, y) = 80 + 10x - 80x^2 + 20y - 80y^2 - 5xy$
2	$\theta(x, y) = [\sin(xy\pi/LW)]^2 + 2\sin(x\pi/L) + 1.5\sin(y\pi/W) + 81$
3	$\theta(x, y) = e^{-(x-0.12)^2} e^{-(y-0.1)^2} / \{(0.012 + 0.1y^5)[\cosh(xy\pi/0.441)]^{0.4}\}$

surface. An objective function of the present inverse problem is thus defined as

$$J = \sum_{i(=I)}^{\bar{m}} \sum_{j(=J)}^{\bar{n}} \left(T_{i,j,\mathrm{NZ}} - \overline{T}_{I,J}\right)^2 \tag{4}$$

Note that the temperatures at the grid points on the outer surface of end plate ($T_{i,j,\mathrm{NZ}}$) are numerically provided by solving the heat conduction equation, and the temperatures at the measurement points ($\overline{T}_{I,J}$) are obtained by experiment. During the iterative process, the temperature distribution at

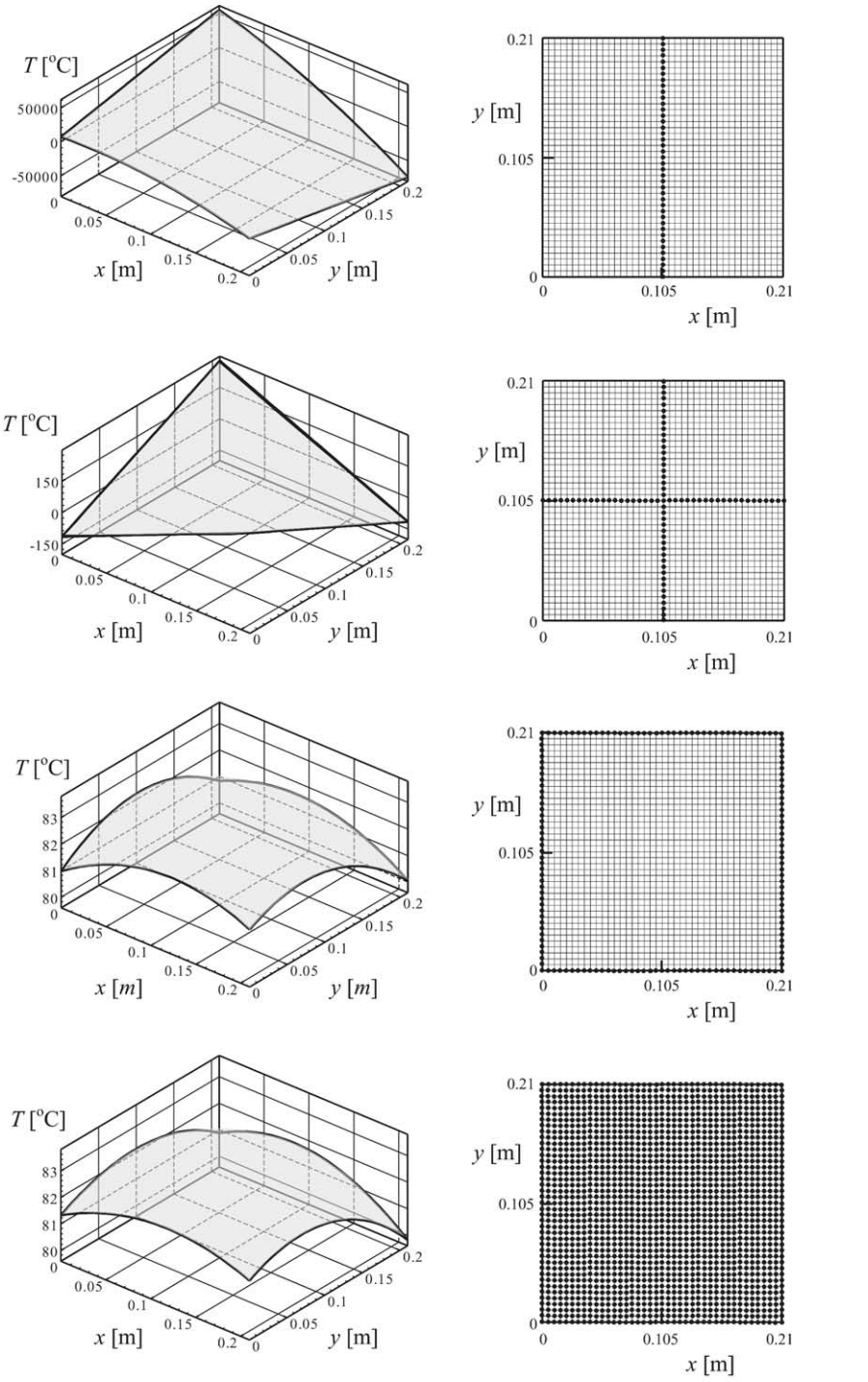

(a) Predicted temperature distribution

(b) Measurement point arrangement

Fig. 2. Temperature predictions with different measurement point arrangements on outer surface of the end plate, for case 3 at σ = 0.1.

the MEA/carbon plate interface is updated iteratively toward minimization of the objective function. Minimization of the objective function means minimization of the difference between $T_{i,j,\mathrm{NZ}}$ and $\overline{T}_{I,J}$. Therefore, the temperature distribution at the MEA/carbon plate interface is obtained, leading to a minimal difference between the numerical and experimental outer surface temperature data.

The temperature distribution $T(x, y)$ at the MEA/carbon plate interface is approximated by a polynomial expression as

$$T(x, y) = a_0 + a_1 x + a_2 x^2 + a_3 y + a_4 y^2 + a_5 xy \quad (5)$$

where a_0, a_1, a_2, a_3, a_4, and a_5 are the undetermined coefficients to be optimized in the iterative process. Different combinations of these coefficients represent different temperature distributions among which the optimal interface temperature distribution may be found. In other words, in the optimization process, the coefficients a_0, a_1, a_2, a_3, a_4, and a_5 are updated iteratively toward the minimization of the object function.

The minimization of the objective function J is accomplished by using the conjugate gradient method. The conjugate gradient method evaluates the gradient functions of the objective function and sets up a new conjugate direction for the updated undetermined coefficients with the help of a direct numerical sensitivity analysis. The method of sensitivity analysis by direct numerical differentiation was first presented by Cheng and Wu [16]. The inverse approach has been proved efficient in the applications for problems with conduction [16] and convection [17]. More recently, it has been used to identify the profile of an unknown interior object in a solid body [18]. In general, the convergence can be attained in a finite number of iterations. The approach is described briefly in the following.

The following is a summary of the sequence of the iterative optimization process for searching the optimal temperature of the MEA/carbon plate interface:

(1) Collect the experimental temperature data on the outer surface of the end plate, $\overline{T}_{I,J}$.
(2) Make an initial guess for the temperature distribution at MEA/carbon plate interface by giving a set of initial values for the undetermined coefficients a_0, a_1, a_2, a_3, a_4, and a_5.

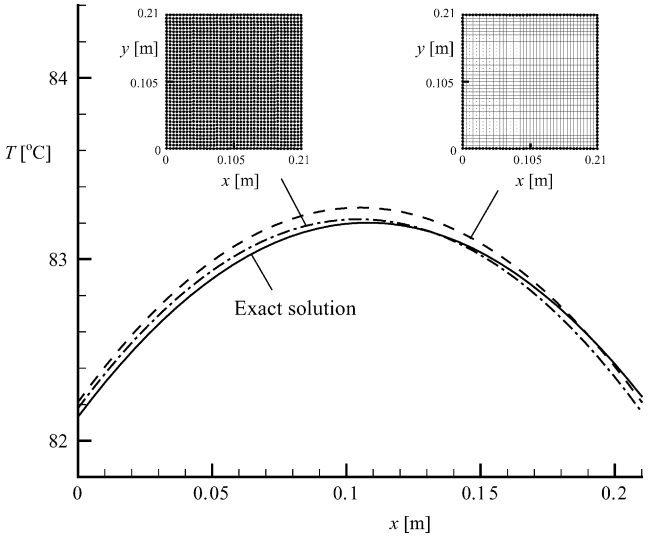

Fig. 3. Predicted temperature profiles along $y = 0.105$ m based on the third and the fourth arrangements considered in Fig. 2.

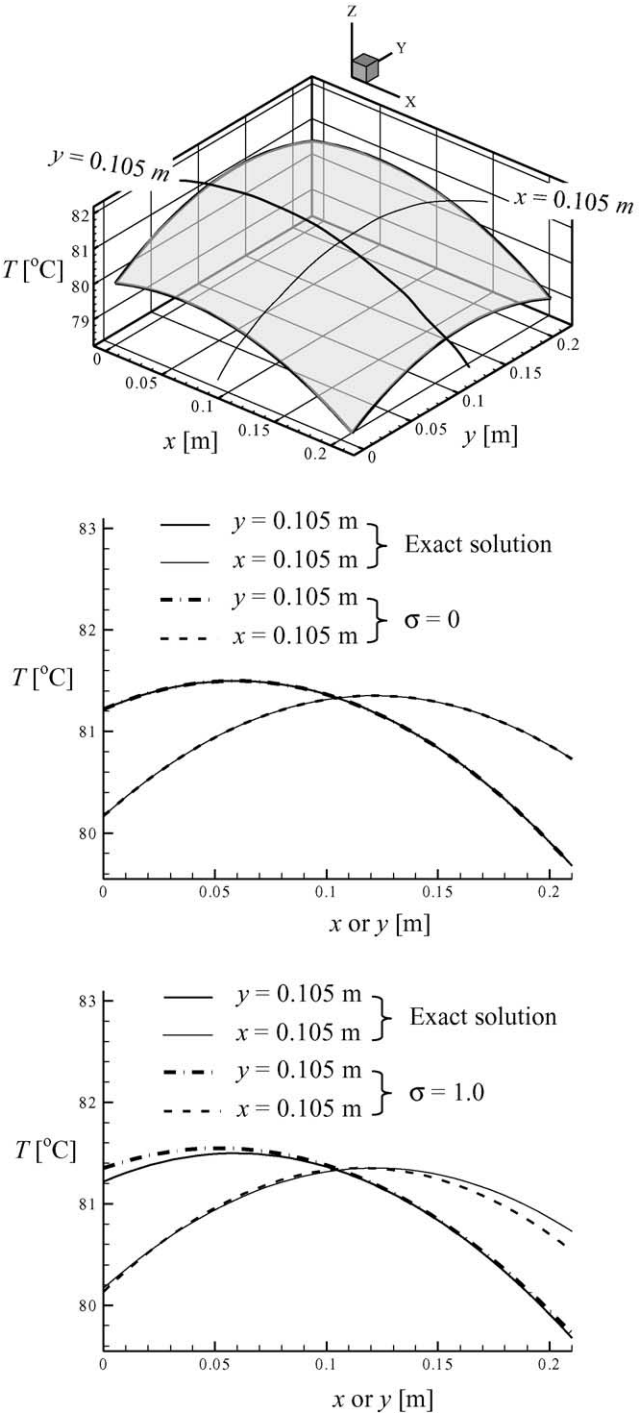

Fig. 4. Effects of experimental uncertainty on accuracy of temperature prediction for case 1.

Table 3
Obtained coefficients at different experimental uncertainties based on 41 × 41 measurement points for case 1

Coefficient	Experimental uncertainty (σ)			
	0	0.1	0.5	1.0
a_0	80.000	80.021	80.083	79.892
a_1	10.000	9.253	9.219	9.976
a_2	−80.000	−76.850	−76.172	−73.074
a_3	20.000	20.170	18.237	23.491
a_4	−80.000	−81.406	−72.575	−91.338
a_5	−5.000	−3.760	−3.578	−22.687
ε [°C]	4.028E−6	1.074E−2	2.624E−2	7.317E−2

(3) Use the heat conduction problem solver to obtain the three-dimensional temperature distribution within the entire fuel cell, and read $T_{i,j,\mathrm{NZ}}$.
(4) Calculate the objective function J by Eq. (4). When the objective function reaches a minimum, the solution process is terminated. Otherwise, proceed to step (5).
(5) Perform the direct numerical sensitivity analysis [16] to determine the gradient functions $\partial J^n/\partial a_i$ (i = 0, 1, ..., 5).
(6) Calculate the conjugate gradient coefficients γ_i^n and the search directions π_i^{n+1} with

$$\gamma_i^n = \left[\frac{(\partial J/\partial a_i)^n}{(\partial J/\partial a_i)^{n-1}}\right]^2, \quad i = 0, 1, \ldots, 5 \tag{6}$$

$$\pi_i^{n+1} = \frac{\partial J^n}{\partial a_i} + \gamma_i^n \pi_i^n, \quad i = 0, 1, \ldots, 5 \tag{7}$$

(7) Calculate the step sizes β_i (i = 0, 1, ..., 5) that lead to $\partial J^{n+1}/\partial \beta_i = 0$, by solving the following simultaneous equations:

$$\begin{aligned}
&\beta_0\pi_0^n \left[\sum_{i=1}^{\bar{m}}\sum_{j=1}^{\bar{n}} \frac{\partial T_{i,j,\mathrm{NZ}}^n}{\partial a_\ell^n}\frac{\partial T_{i,j,\mathrm{NZ}}^n}{\partial a_0}\right] + \beta_1\pi_1^n \\
&\times \left[\sum_{i=1}^{\bar{m}}\sum_{j=1}^{\bar{n}} \frac{\partial T_{i,j,\mathrm{NZ}}^n}{\partial a_\ell^n}\frac{\partial T_{i,j,\mathrm{NZ}}^n}{\partial a_1}\right] + \cdots + \beta_5\pi_5^n \\
&\times \left[\sum_{i=1}^{\bar{m}}\sum_{j=1}^{\bar{n}} \frac{\partial T_{i,j,\mathrm{NZ}}^n}{\partial a_\ell^n}\frac{\partial T_{i,j,\mathrm{NZ}}^n}{\partial a_5}\right] \\
&= \sum_{i=1}^{\bar{m}}\sum_{j=1}^{\bar{n}} \left[(T_{i,j,\mathrm{NZ}}^n - \bar{T}_{I,J})\frac{\partial T_{i,j,\mathrm{NZ}}^n}{\partial a_\ell^n}\right] \\
&\ell = 0, 1, \ldots, 5
\end{aligned} \tag{8}$$

(8) Update the undetermined coefficients with

$$a_i^{n+1} = a_i^n - \beta_i\pi_i^{n+1}, \quad i = 0, 1, \ldots, 5 \tag{9}$$

and go to step (3).

2.3. Simulated experimental data

In this study, the temperature measurement data on the outer surface of the end plate ($\bar{T}_{I,J}$) are simulated by adding a perturbation to the exact temperature distribution on the outer surface. That is,

$$\bar{T}_{I,J} = (T_{i,j,\mathrm{NZ}})_{\mathrm{ex}} + \sigma r_{i,j} \tag{10}$$

where $(T_{i,j,\mathrm{NZ}})_{\mathrm{ex}}$ is the exact temperature distribution at the grid points located at the same positions as the same measurement points on the outer surface of the end plate with a specified interface temperature distribution of interest; $r_{i,j}$ is a random number evenly distributed between −1 and 1 and is provided by a random number generator; and σ is a value given to simulate the uncertainty in the measurement. Note that at σ = 0, the exact outer surface temperature solution $(T_{i,j,\mathrm{NZ}})_{\mathrm{ex}}$, is used directly for the interface temperature prediction.

3. Results and discussion

In order to investigate the validity of the present approach, three different cases with different forms of the exact solution are specified to be predicted, as can be seen in Table 2. There are three major parameters affecting the accuracy of temperature prediction considered in this report. They are: (1) the arrangement and positions of the measurement points; (2) the experimental uncertainty; and (3) the number of measurement points. Meanwhile, the possibility of temperature prediction based on the temperature data on the edge surfaces of the carbon plate is also tested. Results obtained by using the temperature data on the carbon plate edges are provided in order to compare with the data obtained by using the temperature data on the outer surface of the end plate. Typically, 41 × 41 × 35 grid points in the solution domain are adopted after a grid-independence test has been performed. That is, NX = 41 and NY = 41. On the other hand, the number of measurement points on the outer surfaces of the end plate or on the carbon plate edges is varied as a parameter.

3.1. Using temperature data on outer surface of the end plate

There are four possible arrangements for the installation of the measurement points on the outer surface of the end plate, which are shown in Fig. 2. The arrangements of measurement points are plotted in the right portion of this figure and the corresponding predicted temperature contours

are shown in the left portion, for case 3 given in Table 2 at $\sigma = 0.1$. In case 3, the exact temperature function is specified by $e^{-(x-0.12)^2}e^{-(y-0.1)^2/\{(0.012+0.1y^5)[\cosh(xy\pi/0.441)]^{0.4}\}}$. As clearly shown in this figure, with the first and the second measurement point arrangements, the approach leads to unrealistic temperature solutions for the MEA/carbon plate interface. Nevertheless, the predicted solutions of the third and the fourth measurement point arrangements appear to be identical to the exact solution. In order to investigate the discrepancy between the solutions obtained from the third and the fourth measurement point arrangements, the temperature profiles along $y = 0.105$ m are plotted and are compared with the specified exact temperature function in Fig. 3. The solid curve in this figure indicates the exact temperature solution. It

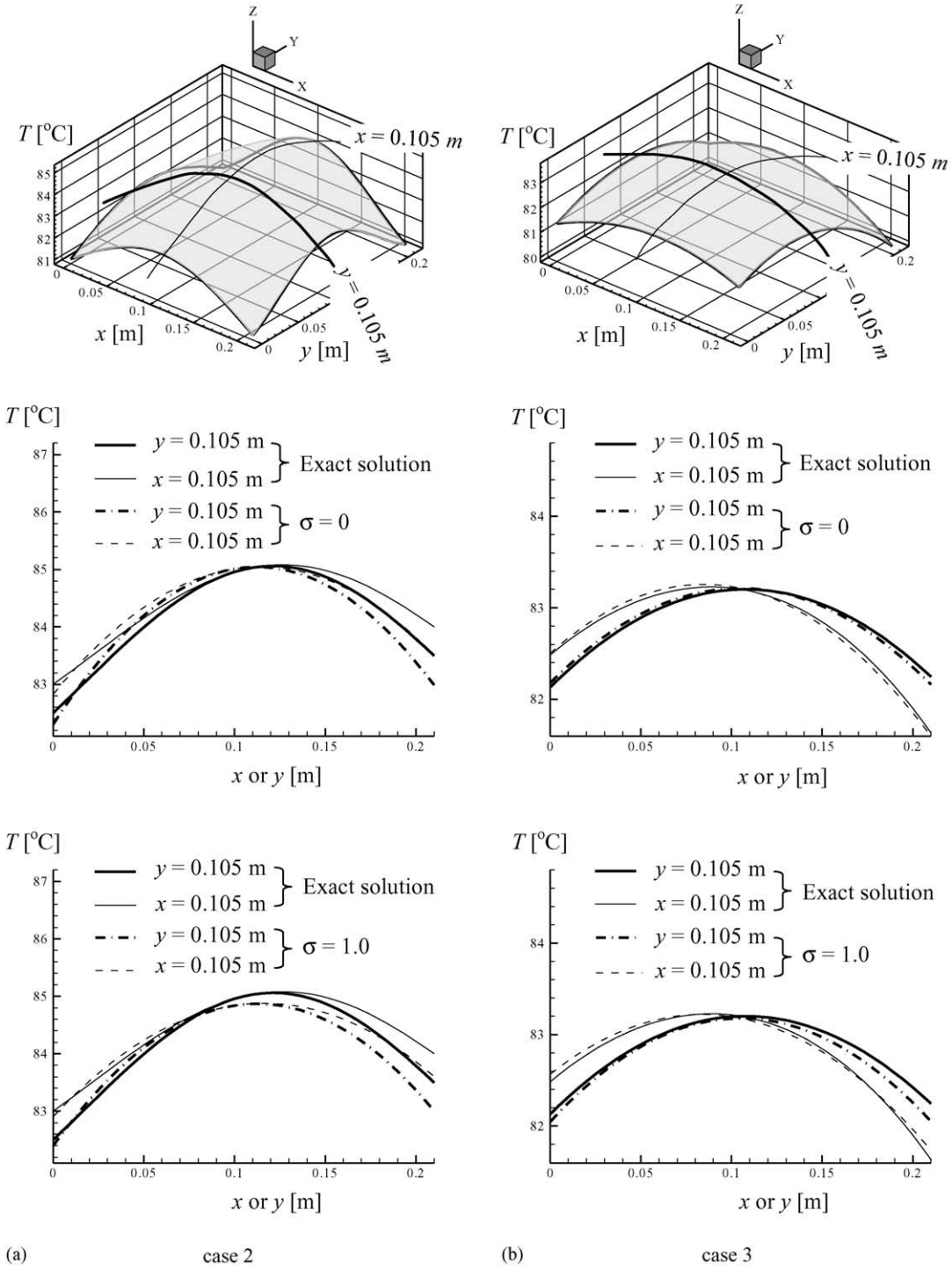

Fig. 5. Effects of experimental uncertainty on the accuracy of temperature prediction for cases 2 and 3.

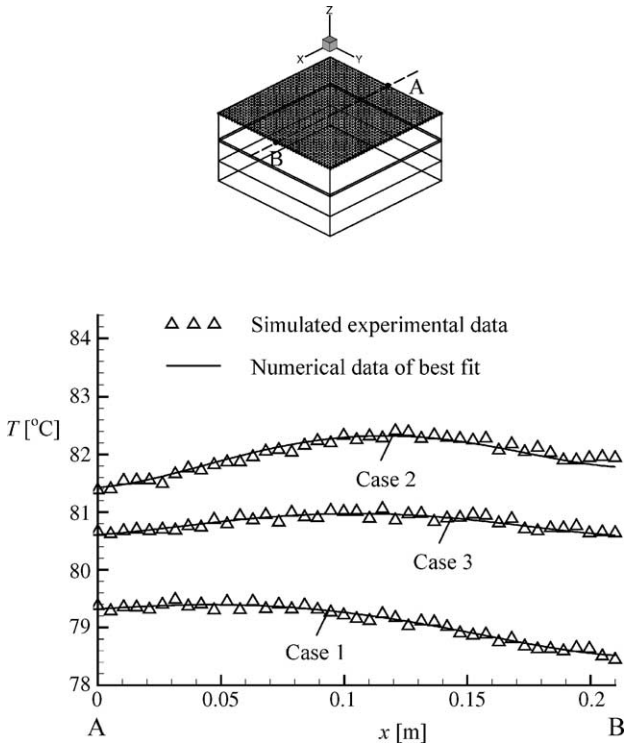

Fig. 6. Numerical data of best fit to the simulated experimental data for temperature distribution on outer surface of end plate along $y = 0.105$ m for cases 1, 2, and 3 at $\sigma = 0.1$.

is found that the third measurement point arrangement results in a greater error in prediction than the fourth arrangement since the former has much less temperature measurement points than the latter. As the accuracy of the temperature prediction is desired, a uniform arrangement of the measurement points like the fourth arrangement is essential. However, if the experiment cost is of major concerns, the third arrangement is still acceptable. In the present study, the fourth arrangement is regarded as standard arrangement for measurement points.

Fig. 4 displays the effects of the uncertainty of the experimental temperature data (σ) on the temperature prediction. In this figure, the exact temperature solution is specified with case 1 of Table 2. The temperature prediction is based on a uniform distributed 41 × 41 measurement points on the outer surface of the end plate. In this case, the exact solution, $\theta(x,y) = 80 + 10x - 80x^2 + 20y - 80y^2 - 5xy$, is a polynomial function. In the upper plot of this figure, the exact temperature function of case 1 is shown. The predicted temperature profiles along $x = 0.105$ m and $y = 0.105$ m are displayed at

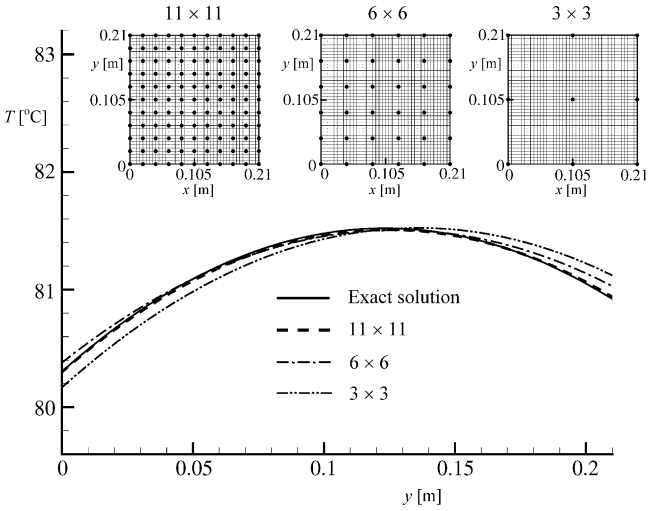

Fig. 7. Effects of number of temperature measurement points on outer surface of end plate on predicted temperature profile along $x = 0.105$ m for case 1 at $\sigma = 0.1$.

$\sigma = 0$ and 1.0. In the lower two plots of this figure, the solid curves indicate the exact solutions and the dashed and dash-dot curves represent the predicted temperature profiles. It is found that at $\sigma = 0$, an accurate temperature prediction can be obtained. However, when a higher uncertainty of $\sigma = 1.0$ is introduced into the experimental temperature data, the deviation between the predicted and the exact temperature data is greatly increased.

To quantify the accuracy of the temperature predictions for the MEA/carbon plate interface, an error norm is defined based on the discrepancy between the predicted and the exact temperature distributions at the MEA/carbon plate interface. That is,

$$\varepsilon = \frac{\sum_{i,j} |(T_{i,j,1}) - \theta_{i,j}|}{(\mathrm{NX} \times \mathrm{NY})} \tag{11}$$

where $T_{i,j,1}$ and $\theta_{i,j}$ denote the predicted and the exact temperature functions at grid (i, j) at the MEA/carbon plate interface and (NX × NY) are the number of grid points on the interface plane. Table 3 shows the obtained undetermined coefficients and the error norms at various uncertainties. In this table, the uncertainty is varied from 0 to 1.0. It is observed that the error norm (ε) of temperature prediction increases with the uncertainty, and the predicted coefficients exhibit greater error as σ is elevated. The error norm ε reaches approximately 0.073 °C at $\sigma = 1.0$. This reveals the accuracy of the present approach.

Table 4
Specific objective functions at different experimental uncertainties for cases 1, 2, and 3

Specific objective function	Case	Experimental uncertainty (σ)			
		0	0.1	0.5	1.0
$\bar{j}$	1	1.535E−11	3.277E−3	8.065E−2	3.251E−1
	2	2.093E−3	5.357E−3	8.160E−2	3.360E−1
	3	1.466E−4	3.438E−3	8.356E−2	3.291E−1

Table 5
Obtained coefficients with different numbers of measurement points on outer surface of end plate for case 1 at $\sigma = 0.1$

Coefficient	Measurement points ($\bar{m} \times \bar{n}$)			
	21 × 21	11 × 11	6 × 6	3 × 3
a_0	79.981	80.010	79.977	79.864
a_1	9.898	9.601	12.403	9.609
a_2	−80.111	−77.594	−90.349	−72.643
a_3	20.531	19.720	18.137	20.965
a_4	−83.164	−78.053	−69.510	−73.430
a_5	−3.502	−5.521	−8.276	−19.134
ε [°C]	1.023E−2	1.045E−2	4.181E−2	7.275E−2

Fig. 5 provides the results of predictions for the non-polynomial exact temperature funcions with cases 2 and 3 based on 41 × 41 measurement points at different uncertainty. The data shown are similar to those given in Fig. 4. However, in Fig. 5, it is seen that even at $\sigma = 0$, for case 2 and 3, the exact temperature curves cannot be fitted exactly by the polynomical temperature distribution like case 1. The error of the temperature prediction with case 2 is greater than that with case 3. The results imply that the magnitude of error is also dependent on the features

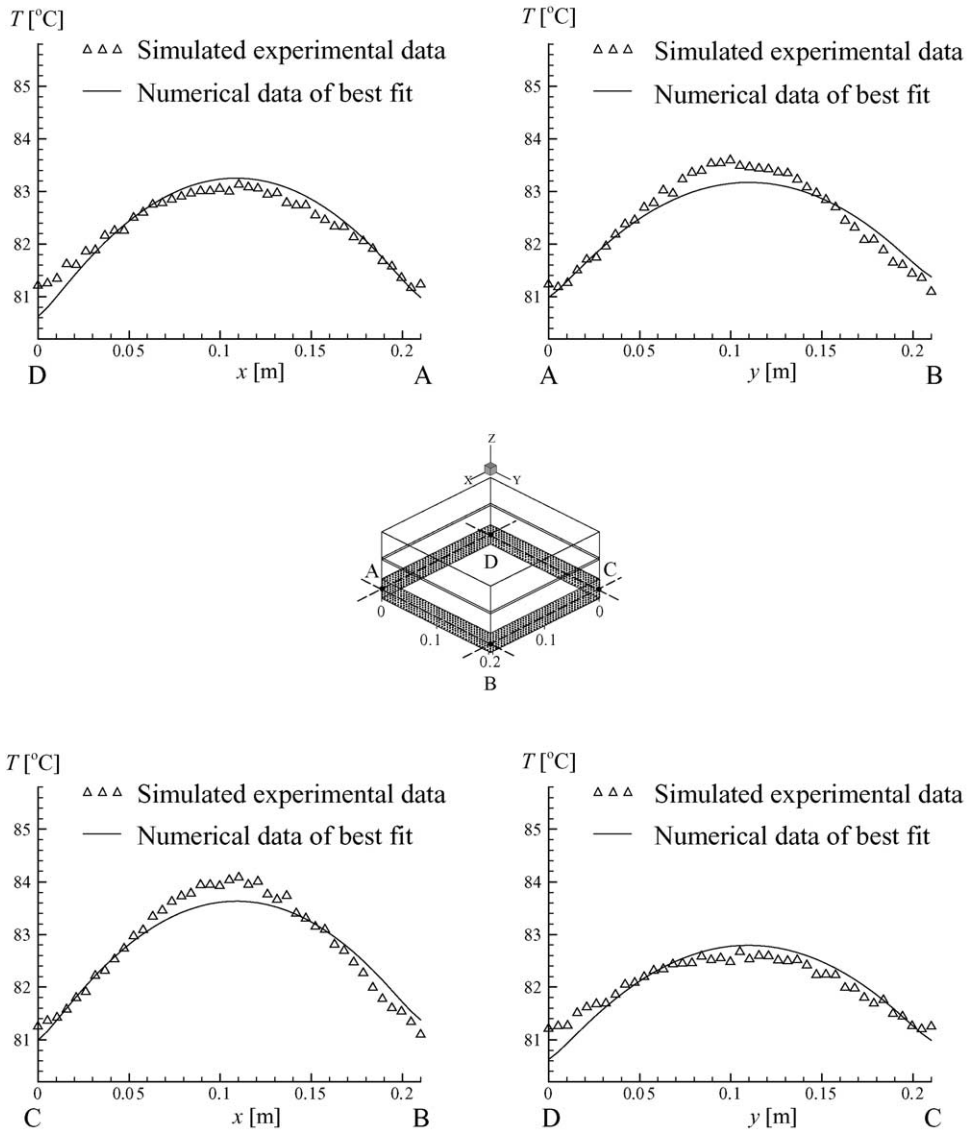

Fig. 8. Numerical data of best fit to the simulated experimental data for temperature distributions on edge surfaces of carbon plate along $z = 0.0015$ m for case 2 at $\sigma = 0.1$.

of temperature distribution at the MEA/carbon plate interface.

On the other hand, a specific objective function is defined in order to evaluate the convergence performance of the method. The specific objective function is defined as

$$\bar{j} = \frac{J}{(\bar{m} \times \bar{n})} \tag{12}$$

where $\bar{m} \times \bar{n}$ is the total number of measurement points on the measured surface.

Fig. 6 shows the comparison between the optimal numerical data and the simulated experimental data for the temperature distribution on the outer surface of the end plate along the y = 0.105 m for cases 1, 2, and 3 at σ = 0.1. From the temperature profiles along y = 0.105 m shown in this figure, it is seen that a best fit can be accurately yielded for each set of the simulated experimental data. Table 4 gives the specific objective function at various experimental uncertainties for cases 1, 2, and 3. Based on the data listed in this table, it can be observed that an increase in uncertainty leads to a higher $\bar{j}$, which represents a worse convergence.

The cost of the experiment is reduced when the number of temperature measurement points is decreased. Therefore, the effects of the number of the measurement points on the outer surface on the accuracy of the temperature prediction for the MEA/carbon plate interface are examined, and part of the results are presented in Fig. 7. In this case, the considered number of measurement points in the x- and y-directions ($\bar{m} \times \bar{n}$) on the outer surface of the end plate is assigned to be 11×11, 6×6, and 3×3. The corresponding positions of the measurement points are plotted in the figure. Meanwhile, the solid curve indicates the exact temperature profile to predict and the dashed, dashdot, and dash-double-dot curves indicate the results obtained from the 11×11, 6×6, and 3×3 measurement points, respectively. It is observed that 11×11 measurement points lead to an accurate prediction of the MEA/carbon plate interface temperature. The discrepancy in the predicted temperature distributions between the exact and the predicted curves is increased as the number of measurement points is reduced.

The dependence of the temperature predictions on the number of measurement points is also shown numerically in Table 5. The obtained coefficients of the interface temperature function are compared with the exact ones. According to the results provided in Table 5, it is found that as the number of measurement points is decreased from 21×21 to 3×3, the error norm ε is elevated from 0.01 to 0.073 °C.

3.2. Using temperature data on edge surfaces of the carbon plate

The possibility of internal temperature prediction based on the temperature data on the edge surfaces of the carbon plate is also studied. Fig. 8 shows comparison between the numerical data of best fit and the simulated experimental data for temperature distribution on the edge surfaces of the carbon plate along z = 0.0015 m for case 2 at σ = 0.1. In this figure, data on four edges (A–B, B–C, C–D, D–A) of the carbon plate are all displayed. Results show that there exists an appreciable discrepancy between the simulated experimental data and the numerical data of best fit. This implies that the convergence of temperature prediction process is relatively poorer when one uses the temperature data on the edge surface of the carbon plate. However, considering the experimental cost reduction, one may still prefer using the temperature data on edge surfaces of the carbon plate rather than using those measured on the end plate surface.

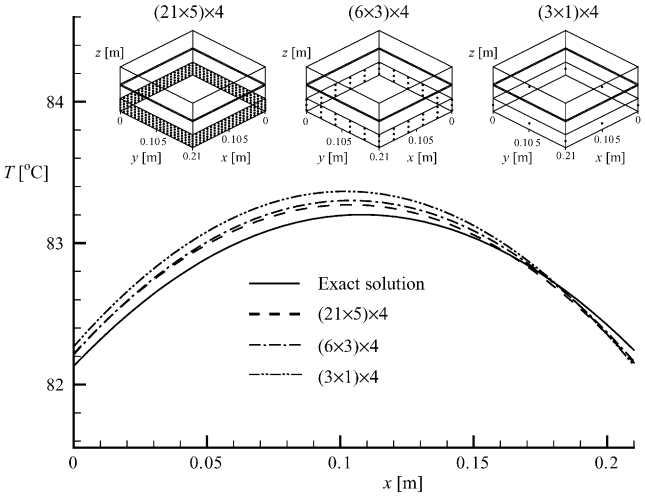

Fig. 9. Effects of number of temperature measurement points on edge surfaces of carbon plate on predicted temperature profile along y = 0.105 m for case 3 at σ = 0.1.

Effects of the number of measurement points on the edge surfaces of the carbon plate on temperature prediction are also investigated. The predicted temperature profiles along y = 0.105 m with different numbers of measurement points for case 3 at σ = 0.1 are shown in Fig. 9. The number of measurement points is represented by $(c \times d) \times 4$ where $c \times d$ represents the number of measurement points on each edge surface and 4 accounts for the four edge surfaces with a carbon plate. In this figure, the number of measurement points is assigned to be $(21 \times 5) \times 4$, $(6 \times 3) \times 4$, and $(3 \times 1) \times 4$, which are also plotted in the figure. Again, it is found that the accuracy of temperature prediction of the internal temperature of the fuel cell is significantly influenced by the number of temperature measurement points on the edge surfaces of the carbon plate.

It is important to mention that the present inverse approach is not limited to the temperature measurement application. Distribution of the current density and gas concentrations inside the fuel cell may also be determined provided that a powerful direct problem solver is available.

4. Concluding remarks

The present study is concerned with temperature predictions of the internal temperature of a fuel cell. The temper-

ature distribution at the MEA/carbon plate interface is predicted based on the measured temperature data on the outer surfaces by an undestructive inverse method. To demonstrate the validity of this approach, three different cases (cases 1–3) with different forms of the exact solution are specified to be predicted, and the temperature measurement data on the outer surfaces are generated by adding a perturbation to the exact temperature distribution on the outer surfaces. Effects of the arrangement and positions of the temperature measurement points, the experimental uncertainty (σ), and the number of measurement points on the internal temperature prediction have been investigated. Meanwhile, the performance of the temperature prediction based on the edge temperature data of the carbon plate is compared with that based on the outer surface temperature data of the end plate. In addition, an error norm (ε) and a specific objective function ($\bar{j}$) have been defined in order to quantify the accuracy and convergence of the approach.

Four possible arrangements of the measurement points are installed on the outer surface of the end plate, and the predicted solutions of the third and the fourth measurement point arrangements appear to be identical to the exact solution. However, the third measurement point arrangement results in a greater error in prediction than the fourth arrangement.

It is found that at $\sigma = 0$, an accurate temperature prediction can be obtained for case 1. However, when a higher uncertainty of $\sigma = 1.0$ is introduced into the experimental temperature data, the deviation between the predicted and the exact temperature data is greatly increased. The error norm ε reaches approximately 0.073 °C at $\sigma = 1.0$.

For cases 2 and 3, even at $\sigma = 0$, the exact temperature curves cannot be fitted exactly by the polynomical temperature distribution like case 1. The results imply that the magnitude of error is also dependent on the features of temperature distribution at the MEA/carbon plate interface.

In addition, the comparison between the best fit numerical data and the simulated experimental data for the temperature distribution on the outer surface shows that a best fit can be accurately yielded for each set of the simulated experimental data. From the specific objective function at various experimental uncertainties for cases 1, 2, and 3, it can be observed that an increase in uncertainty leads to a higher $\bar{j}$, which represents a worse convergence.

Meanwhile, 11×11 measurement points are sufficient to provide an accurate prediction of the MEA/carbon plate interface temperature. The discrepancy in the predicted temperature distributions between the exact and the predicted curves is increased as the number of measurement points is reduced. As the number of measurement points is decreased from 21×21 to 3×3, the error norm ε is elevated from 0.01 to 0.073 °C.

As for the temperature prediction based on the edge temperature data of the carbon plate, it is found that the convergence of temperature prediction process is relatively poor when one uses the temperature data on the edge surfaces of the carbon plate, instead of the temperature data on the end plate surface, and the accuracy of temperature prediction of the internal temperature of the fuel cell is significantly influenced by the number of temperature measurement points on the edge surfaces of the carbon plate.

References

[1] K.H. Choi, D.H. Peck, C.S. Kim, D.R. Shin, T.H. Lee, Water transport in polymer membranes for PEMFC, J. Power Sources 86 (2000) 197–201.

[2] N. Djilali, D. Lu, Influence of heat transfer on gas and water transport in fuel cells, Int. J. Therm. Sci. 41 (2002) 29–40.

[3] D. Natarajan, T.V. Nguyen, Three-dimensional effects of liquid water flooding in the cathode of a PEM fuel cell, J. Power Sources 115 (2003) 66–80.

[4] R.K.A.M. Mallant, PEMFC systems: the need for high temperature polymers as a consequence of PEMFC water and heat management, J. Power Sources 118 (2003) 424–429.

[5] D. Chu, R. Jiang, Comparative studies of polymer electrolyte membrane fuel cell stack and single cell, J. Power Sources 80 (1999) 226–234.

[6] S. Giddey, F.T. Ciacchi, S.P.S. Badwal, Design, assembly and operation of polymer electrolyte membrane fuel cell stacks to 1 kW_e capacity, J. Power Sources 125 (2004) 155–165.

[7] R. Jiang, D. Chu, Stack design and performance of polymer electrolyte membrane fuel cells, J. Power Sources 93 (2001) 25–31.

[8] E. Hontañón, M.J. Escudero, C. Bautista, P.L. García-Ybarra, L. Daza, Optimisation of flow-field in polymer electrolyte membrane fuel cells using computational fluid dynamics techniques, J. Power Sources 86 (2000) 363–368.

[9] P.W. Li, L. Schaefer, Q.M. Wang, T. Zhang, M.K. Chyu, Multi-gas transportation and electrochemical performance of a polymer electrolyte fuel cell with complex flow channels, J. Power Sources 115 (2003) 90–100.

[10] M. Krumpelt, T.R. Krause, J.D. Carter, J.P. Kopasz, S. Ahmed, Fuel processing for fuel cell systems in transportation and portable power applications, Catal. Today 77 (2002) 3–16.

[11] J.M. Zalc, D.G. Löffler, Fuel processing for PEM fuel cells: transport and kinetic issues of system design, J. Power Sources 111 (2002) 58–64.

[12] J. Yuan, M. Rokni, B. Sundén, Simulation of fully developed laminar heat and mass transfer in fuel cell ducts with different cross-sections, Int. J. Heat Mass Transfer 44 (2001) 4047–4058.

[13] A. Kumar, R.G. Reddy, Effect of channel dimensions and shape in the flow-field distributor on the performance of polymer electrolyte membrane fuel cells, J. Power Sources 113 (2003) 11–18.

[14] S. Um, C.Y. Wang, Three-dimensional analysis of transport and electrochemical reactions in polymer electrolyte fuel cells, J. Power Sources 125 (2004) 40–51.

[15] P. Moin, Fundamentals of Engineering Numerical Analysis, Cambridge University Press, New York, 2001.

[16] C.H. Cheng, C.Y. Wu, An approach combining body-fitted grid generation and conjugate gradient methods for shape design in heat conduction problems, Numer. Heat Transfer, Part B 37 (2000) 69–83.

[17] C.H. Cheng, M.H. Chang, Shape design for a cylinder with uniform temperature distribution on the outer surface by inverse heat transfer method, Int. J. Heat Mass Transfer 46 (2003) 101–111.

[18] C.H. Cheng, M.H. Chang, Shape identification by inverse heat transfer method, J. Heat Transfer 125 (2003) 224–231.